International Journal of Applied Earth Observation and Geoinformation 118 (2023) 103250

Contents lists available at ScienceDirect

International Journal of Applied Earth Observation and Geoinformation

journal homepage: www.elsevier.com/locate/jag

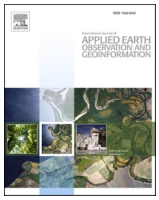

A semi-analytical radiative transfer model for explaining soil spectral features

Fuyu Wu [a], Kun Tan [b,c,d,*], Xue Wang [b,c,d], Jianwei Ding [e], Zhaoxian Liu [e], Bo Han [f]

[a] Key Laboratory for Land Environment and Disaster Monitoring of NASG, China University of Mining and Technology, Xuzhou 221116, China
[b] Key Laboratory of Geographic Information Science (Ministry of Education), East China Normal University, Shanghai 200241, China
[c] Key Laboratory of Spatial-temporal Big Data Analysis and Application of Natural Resources in Megacities, Ministry of Natural Resources, East China Normal University, Shanghai 200241, China
[d] School of Geographic Sciences, East China Normal University, Shanghai 200241, China
[e] Second Surveying and Mapping Institute of Hebei, Shijiazhuang 050037, China
[f] Institute of Remote Sensing Satellite, China Academy of Space Technology, Beijing 100094, China

ARTICLE INFO

Keywords:
Soil multifactor radiative transfer model
Absorption and scattering coefficients
Spectral features

ABSTRACT

Spectral techniques play a key role in the estimation of large-scale soil parameters, but most of the current estimation models are data-driven models lacking a physical basis. Therefore, in this study, we developed a novel radiative transfer model named the soil multifactor radiative transfer (SMRT) model that predicts the soil spectra as a function of the soil organic matter (SOM), particle size distribution (PSD), and iron oxide content. The SMRT model explains the soil spectral features commonly used in the data-driven estimation models and can be used to explore the mechanisms by which soil-related parameters affect soil spectra according to the model parameters. A total of 79 soil profile datasets were used in the experiments conducted in this study. The reflectance of the soil after air-drying can ignore the effect of moisture, thereby ensuring that the main influences on the soil spectra are the SOM, iron oxide content, and PSD. The SMRT model performed very well in the spectral simulation (R^2 = 0.9681, *RMSE* = 0.0266, *MAE* = 0.0160). The absorption and scattering coefficients of the SMRT model explain the radiative transfer mechanism for the color representation of black soil and laterite soil. The spectral features around 1910 nm and 2210 nm are caused by not only the soil moisture (SM) and clay mineral content, but several other factors, including the SOM, iron oxide content, and PSD. Overall, these findings show that the SMRT model has a superior ability to describe the soil radiative transfer processes. However, as the coefficients in the SMRT model are dependent on the soil properties, the coefficients should be calibrated by an optimization algorithm and cannot be constants, which leads to the requirement for soil samples to calibrate the coefficients in practical applications.

1. Introduction

Soil is a crucial component in many ecosystems and plays a key role in agricultural systems (Wei et al. 2021). A primary concern regarding soil is the analysis of the soil element content (Liu et al. 2020). Traditional soil analysis is carried out using large-scale sample collection and laboratory analysis, which are both intensive and time-consuming (Anne et al. 2014, Chen et al. 2021, Tan et al. 2021). Soil spectral information can provide the combined information of multiple soil constituents (Sawut et al. 2018, Wang et al. 2018). It is now well established, from a variety of studies, that soil reflectance spectroscopy is an efficient, rapid, and wide-scale technique, compared with traditional laboratory analysis (Song et al. 2015, Peng et al. 2019).

Much of the soil spectral analysis research has focused on predicting soil properties such as soil organic matter (SOM) (Wang et al. 2010, Angelopoulou et al. 2019), soil moisture (SM) (Zhang et al. 2020), texture (Benedet et al. 2020), nutrients (Cai et al. 2021), and heavy metals (Sun and Zhang 2017, Jeong et al. 2021, Yin et al. 2021). Although many studies of soil spectral analysis have achieved good results based on data-driven models and have specified the sensitive wavelengths corresponding to soil properties, the physical mechanism theory is lacking in the estimation process (Chen et al. 2022). The primary reason for this is that soil is a complicated object consisting of organic matter, minerals, water, and air, and its radiative transfer

* Corresponding author at: Key Laboratory of Geographic Information Science (Ministry of Education), East China Normal University, Shanghai 200241, China.
E-mail address: tankuncu@gmail.com (K. Tan).

https://doi.org/10.1016/j.jag.2023.103250
Received 30 September 2022; Received in revised form 20 February 2023; Accepted 25 February 2023
Available online 6 March 2023

processes are difficult to simulate.

It is now established from a variety of studies that soil spectra are mainly affected by the soil-forming parent material (Demattê and da Silva Terra 2014), the SM (Koch et al. 2021), the SOM (Liu et al. 2018), the soil iron oxide, the particle size distribution (PSD) (Janik et al. 2020), and the measurement conditions (Stenberg et al. 2010). Therefore, considering the main influencing factors for soil spectra, scholars have carried out a series of studies using physical radiative transfer (RT) models. The Hapke model, multi-flux model, and beam tracing (BT) model are commonly used to illustrate the soil RT process. The Hapke model assumes that the total radiance is decomposed into single and multiple scattering radiance. Jacquemoud et al. (1992) proposed the SOILSPECT model describing the directional reflectance spectra of wet soils and air-dried soils. Liang and Townshend (1996) improved the Hapke model and considered that the total radiance is the sum of three parts, i.e., single, double, and multiple scattering radiance, which significantly improved the simulation accuracy. Labarre et al. (2017) retrieved simulated soil surface roughness from multi-angular reflectance data by a Hapke-based model. Ding et al. (2022) compared the SOILSPECT model and the original Hapke model in fitting field soil and air-dried soil bidirectional reflectance and found that both models showed a good performance. Meanwhile, they also extended the Hapke model by incorporating the asymptotic RT model to estimate SM. However, the assumptions of the Hapke model constrain its application for the estimation of SM, and the model cannot explain the effects of SOM and soil iron oxide content on soil spectra.

The Kubelka-Munk (KM) model was introduced into soil spectra by Barrón and Torrent (1986) for describing the soil spectral response of iron oxide content on color and to predict the hematite and goethite contents from soil spectra. Sadeghi et al. (2015) presented a KM-based physical model to estimate the SM from laboratory control variable experiments based on wet soil. The KM model simplifies the RT process by considering only the fluxes in the upper and lower directions. It also considers the soil absorption and scattering coefficients as a linear weighted sum of the multiple substances in the soil, meaning that it is of great importance in soil component estimation.

The BT model, unlike the approximate and numerical solutions of the KM model, computes a solution to the RT process based on the reflected and refracted light, according to the Fresnel equations and Snell's law, respectively. Bablet et al. (2018) proposed the multilayer radiative transfer model of soil reflectance (MARMIT) based on the light reflection and refraction in different mediums and assumed that natural wet soil is a layer of dry soil covered with a water film, to estimate SM content from soil spectral reflectance. Sadeghi et al. (2018) considered the air-dried soil total reflectance as the sum of the surface and volume reflectance and calculated these values using the BT model according to soil samples with different single particle sizes. They then extended the model by integration to describe the reflectance of nonuniform air-dried soil and concluded that the reflection spectra of soil mainly focus on the surface information, and that depth information rarely exceeds 1 mm, based on their experimental results (Norouzi et al. 2021). However, such studies remain narrow in focus as they dealt with only a single soil property by controlled variable experiments, without integrating the main influencing factors on the soil spectra.

In this paper, a novel physical model named the soil multifactor radiative transfer (SMRT) model is proposed to explain the soil spectral features commonly used in soil estimation models in terms of RT. The new model considers the various factors affecting soil spectra, such as SOM, iron oxide content, and PSD. The response mechanisms between the reflectance and SOM, iron oxide content, and PSD were investigated by analyzing the absorption and scattering coefficients of soil properties. In addition, unlike the control variable experiments often used in the previous studies, we used soil profile data, with consistent soil-forming parent materials and some differences in SOM and iron oxide content under the same profile, to give a more realistic picture of the soil spectra influencing mechanism.

2. Method

2.1. Soil multifactor radiative transfer (SMRT) model

The SMRT model is derived based on the KM model and adequately considers the scattering and absorption coefficients of SOM, PSD, and soil iron oxide to describe the soil RT processes. Fig. 1 shows that the KM model ignores the complex phenomenon of reflection and refraction in the soil medium and only considers the light flux in two directions, i.e., downwards and upwards, perpendicular to the soil layer.

The KM model, which is a rigorous radiative equation derivation, has good physical meaning in simple situations (Christy et al. 1995). Although the KM model assumes isotropic light scattering, it has been experimentally shown to achieve satisfactory results under the assumption of non-isotropic conditions. In the KM model, a pair of coupled differential equations are proposed to describe the radiance I and J as follows:

$$dI(\xi,\varphi) = -(K+S)I(\xi,\varphi)d\varphi + SJ(\xi,\varphi)d\varphi \tag{1}$$

$$dJ(\xi,\varphi) = (K+S)J(\xi,\varphi)d\varphi - SI(\xi,\varphi)d\varphi \tag{2}$$

where φ represents the depth in the layer; ξ represents the wavelength; and S and K represent the scattering and absorption coefficients, respectively (Vargas and Niklasson 1997). The analytical solution for the reflectance R and transmittance T can be given by Equations (3) and (4):

$$R = \frac{(1-\beta^2)(exp(\alpha d) - exp(-\alpha d))}{(1+\beta)^2 exp(\alpha d) - (1-\beta)^2 exp(-\alpha d)} \tag{3}$$

$$T = \frac{4\beta}{(1+\beta)^2 exp(\alpha d) - (1-\beta)^2 exp(-\alpha d)} \tag{4}$$

where $\alpha \equiv \sqrt{K(K+2S)}$, $\beta \equiv \sqrt{K/(K+2S)}$, and d represents the soil layer depth. As the soil layer depth becomes thicker, the transmittance gradually tends to zero and the reflectance gradually increases and stabilizes to a fixed value, which is called the infinite reflectance R_∞(Ciani et al. 2005). Thus, Equation (3) can be rewritten as follows:

$$R_\infty = \frac{(1-\beta)}{(1+\beta)} = 1 + \frac{K}{S} - \sqrt{\left(\frac{K}{S}\right)^2 + 2\frac{K}{S}} \tag{5}$$

The scattering and absorption coefficients for mixed substances in KM models are often considered to be the proportionally weighted sum of the scattering and absorption coefficients for each substance. In this study, for soil samples under the same profile, it was assumed that the samples had a consistent soil-forming parent material and that the main

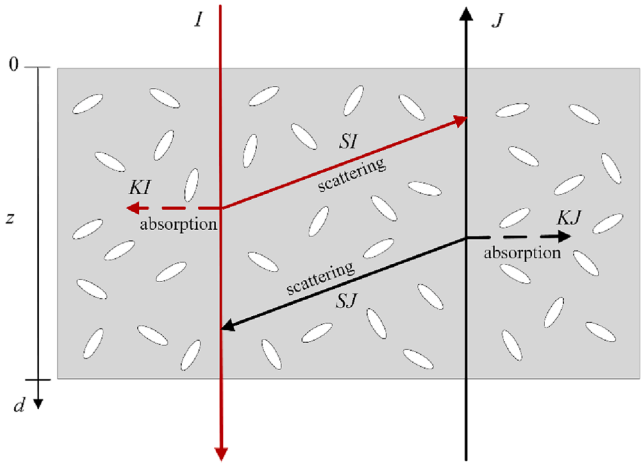

Fig. 1. KM model illustration sketch.

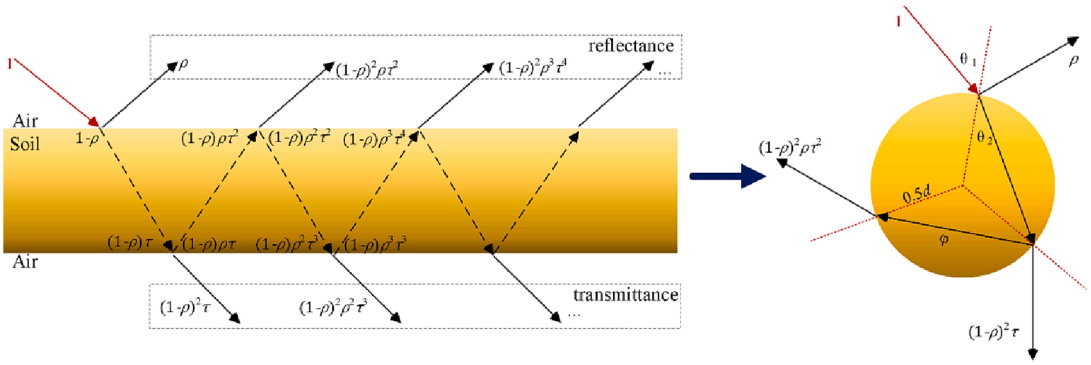

Fig. 2. Sketch illustrating the reflection and transmission of soil particles, where ρ is the reflectivity and τ is the transmissivity.

factors affecting the spectra were the SOM, iron oxide content, PSD, and SM content.

In this study, the soil used for the laboratory experiments was air-dried soil, so that the effect of SM could be ignored. Thus, given this assumption, the absorption coefficient K_{Soil} and scattering coefficient S_{Soil} of the total soil can be described as:

$$K_{Soil} = K_{Par}(1 - \theta_{Som} - \theta_{SIO}) + K_{Som}\theta_{Som} + K_{SIO}\theta_{SIO} \tag{6}$$

$$S_{Soil} = S_{Par}(1 - \theta_{Som} - \theta_{SIO}) + S_{Som}\theta_{Som} + S_{SIO}\theta_{SIO} \tag{7}$$

where K, S, and θ represent the absorption coefficient, scattering coefficient, and content, respectively, and the subscripts *Par*, *SOM*, and *SIO* represent soil particles, SOM, and soil iron oxide, respectively. K_{Par} and S_{Par} are calculated by accumulating the reflectance r and transmittance t of multiple monolayers of particles based on the BT model (Banninger and Fluhler 2004). Assuming that the intensity of the incident beam is 1, then a fraction of the beam is reflected into the air from the soil surface with reflectivity ρ, and another fraction enters the soil layer with an intensity of $1-\rho$. Due to soil layer absorption, the beam intensity at the interface of the medium will become $(1-\rho)\tau$ after passing through the soil layer, where τ is the transmissivity. The intensity of the beam entering the air again after passing through the soil layer is $(1-\rho)^2\tau$. Thus, the total reflectance r and transmittance t can be calculated as:

$$r = \rho + (1-\rho)^2\rho\tau^2 + (1-\rho)^2\rho^3\tau^4 + \cdots = \rho + \frac{(1-\rho)^2\rho\tau^2}{1-\rho^2\tau^2} \tag{8}$$

$$t = (1-\rho)^2\tau + (1-\rho)^2\rho^2\tau^3 + \cdots = \frac{(1-\rho)^2\tau}{1-\rho^2\tau^2} \tag{9}$$

The total reflectance r and transmittance t of a thin layer can be transformed into soil particles based on the Beer-Lambert law.

$$\tau = exp(-k\varphi) \tag{10}$$

$$r = \rho + \frac{(1-\rho)^2\rho exp(-2k\varphi)}{1-\rho^2 exp(-2k\varphi)} \tag{11}$$

$$t = \frac{(1-\rho)^2 exp(-k\varphi)}{1-\rho^2 exp(-2k\varphi)} \tag{12}$$

where k represents the linear absorption coefficient, and φ is the length of the beam inside the soil layer. According to the conclusions of Sadeghi et al. (2015), φ can be approximated as being equal to the particle size d.

Due to the form of the measured particle size results, probability accumulation is used in this model instead of the integration form to describe soils with a nonuniform PSD under natural conditions (Norouzi et al. 2021).

$$r^* = \sum_i^n r(\rho, k, d_i)P_i \tag{13}$$

$$t^* = \sum_i^n t(\rho, k, d_i)P_i \tag{14}$$

where P_i is the probability of particle size d_i. Thus, K_{Par} and S_{Par} are calculated by multiplying the absorption and scattering of a single level by the number of levels per unit depth N (Banninger and Fluhler 2004).

$$K_{Par} = N^*(1 - r^* - t^*) \tag{15}$$

$$S_{Par} = N^* r^* \tag{16}$$

The reflection spectra of soil mainly focus on the surface information, and the depth information rarely exceeds 1 mm (Norouzi et al. 2021). Thus, the unit of length in the model is standardized in millimeters, and the approximate value of N is 100, according to the average particle size of the soil.

2.2. Solutions for the model parameters

The soil particle optical coefficients (ρ and k), absorption coefficients (K_{SOM} and K_{SIO}), and scattering coefficients (S_{SOM} and S_{SIO}) need to be determined. Although the parameters can be solved by control variable experiments, the complexity makes the SMRT model impractical for future applications. To streamline the solution of the SMRT model, a genetic algorithm (GA) is used to fit the parameters.

A GA is an optimization method based on the population, and is inspired by natural selection (Holland 1992). The new population is produced by iterative use of genetic operators on the individuals present in the population according to the chromosome representation, selection, crossover, mutation, and fitness function computation. GAs have a superior global search capability because they can evaluate multiple individuals and produce multiple optimal solutions (Katoch et al. 2021). In the SMRT model, the *RMSE* of the simulated spectral reflectance is defined as the fitness function.

In the laboratory experiments, two of the three samples under each profile were selected randomly to determine the model parameters, and the one remaining sample was used to verify the validity of the SMRT model. Fig. 3 provides an illustration of the SMRT model.

2.3. Evaluation method

To evaluate the performance of the SMRT model, the root-mean-square error (*RMSE*), root-mean-square error percentage (*RMSEP*), the coefficient of determination (R^2), and the mean absolute error (*MAE*), which are expressed as shown in Equations (17)–(20), respectively, are used in this paper (Ou et al. 2021).

$$RMSE = \sqrt{\frac{\sum_{i=1}^n (y_i - \hat{y}_i)^2}{n}} \tag{17}$$

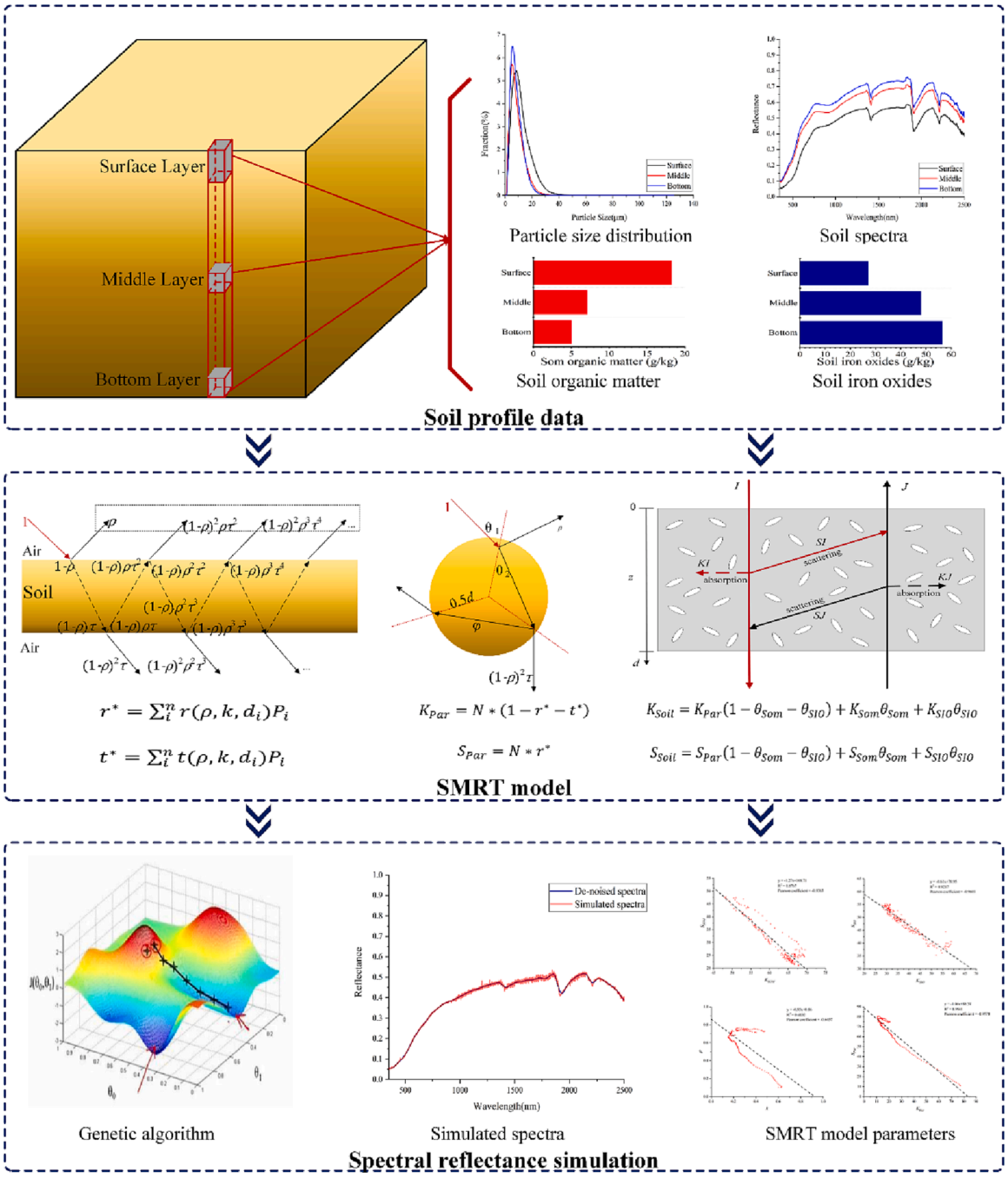

Fig. 3. Illustration of the SMRT model.

$$RMSEP = \frac{RMSE}{y_{i\_max}} * 100\% \tag{18}$$

$$R^2 = 1 - \frac{\sum_{i=1}^{n}(y_i - \widehat{y_i})^2}{\sum_{i=1}^{n}(y_i - \overline{y_i})^2} \tag{19}$$

$$MAE = \frac{\sum_{i=1}^{n}|y_i - \widehat{y_i}|}{n} \tag{20}$$

where y_i is the observed spectral reflectance, y_{i_max} is the observed maximum of the spectral reflectance of all the samples, and $\widehat{y_i}$ is the spectral reflectance simulated using the SMRT model.

3. Experimental data

3.1. Study area

To evaluate the capability of the SMRT model to describe the soil RT process, we relied on 79 soil profiles, each of which was sampled at three depths of 0–20 cm (surface layer), 50 cm (middle layer), and 100 cm (bottom layer), according to Chinese industry standards (HJ/T 166–2004). The sampling area was in Yitong Manchu Autonomous County, Jilin province, China. A soil auger was used to collect the soil profile samples during May 1 to 5, 2019 (Fig. 4). Finally, 237 samples were desiccated, pulverized with a pestle, screened by a 0.15 mm sieve, and divided into four parts for measuring the laboratory spectra, PSD, SOM, and iron oxide content.

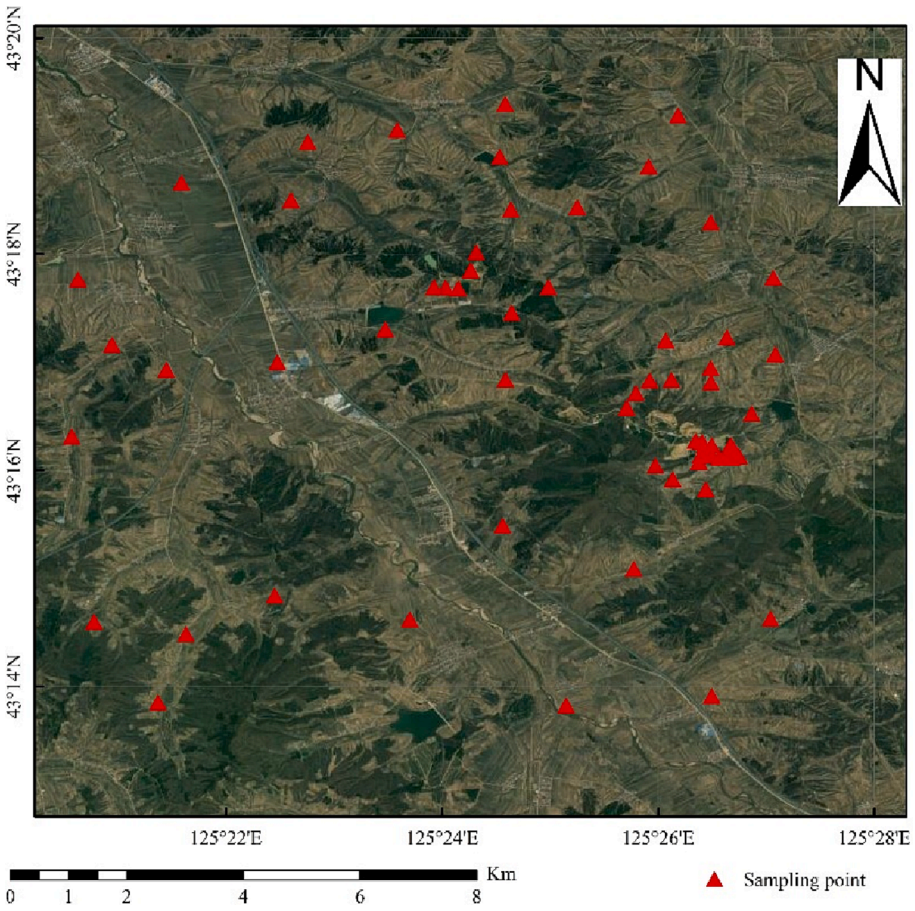

Fig. 4. Sampling point locations in the study area.

3.2. Reflectance measurements

Each soil sample was measured by the use of an ASD FieldSpec III Pro FR spectroradiometer with a 25° field of view in a darkroom. The spectroradiometer resolution is 2 nm in the visible and near-infrared (VNIR) range and 10 nm in the short-wave infrared (SWIR) range. The spectroradiometer and lamp were pre-warmed for 40 min prior to the measurements, which reduces systematic errors in the spectral measurements and the breakpoint effect caused by the two sensors.

During the measurement process, the soil samples were placed in Petri dishes with a diameter of 9 cm and a depth of 2 cm. The surface of each soil sample was flattened to reduce the effect of shadows. A 1000-lumen halogen lamp with a zenith angle of 45° at a distance of 40 cm from the sample was used as the light source. The detection fiber probe was placed vertically to the soil sample at a distance of 15 cm for observation. The illumination and view angle were fixed to ensure consistency of the measured spectra, and a barium sulfate panel was used every 15 min to optimize the spectroradiometer. The average value of five measurements was considered as the final soil spectra, which minimizes systematic errors. Fig. 5 shows the range of the spectra and the average spectrum measured in the laboratory.

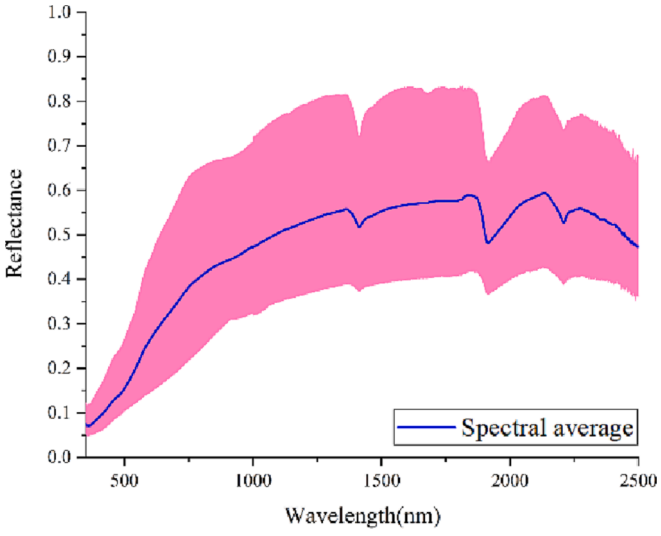

Fig. 5. Soil spectra.

3.3. Soil property measurement

Laboratory tests were performed for the main factors of the soil spectra involved in the SMRT model, i.e., PSD, SOM, and soil iron oxide content. The soil PSD was measured using a Rise-2006 laser diffraction particle size analyzer, which covers a particle size of 0.05–800 μm. The soil iron oxide concentration was measured by inductively coupled plasma-mass spectrometry (ICP-MS), and the SOM content was measured by the potassium dichromate method.

3.4. ICRAF-ISRIC spectral library

The ICRAF-ISRIC soil spectral library contains spectra of 4438 air-dried soil samples and the associated property data. The samples are from 58 countries in Africa, Asia, Europe, North America, and South America, and cover a wide range of soil types (Garrity and Bindraban

2004). The soil spectra were recorded using a FieldSpec FR spectroradiometer at wavelengths of 350–2500 nm. As the ICRAF-ISRIC spectral library does not provide soil PSD data, which is one of the critical parameters in the SMRT model, we employed the soil texture estimation data provided by Rossel et al. (2016) as the substitute soil PSD data. Soil texture data can be derived from soil PSD data (Shirazi and Boersma 1984), which means that soil PSD can be simply replaced by soil texture data when calculating the absorption and scattering coefficients of soil particles. Accordingly, the particle size d_i in Equations (13) and (14) in the SMRT model was simplified to the clay, silt, and sand average particle size. Soil profile data which had the same soil-forming parent material were selected from the ISRIC spectral library to validate the SMRT model. Finally, 328 effective soil profiles from 46 countries were selected, with a total of 2401 soil samples. Table 1 lists the number of soil profiles and soil samples for each country. Fig. 6 shows the range of the selected spectra and the average spectrum.

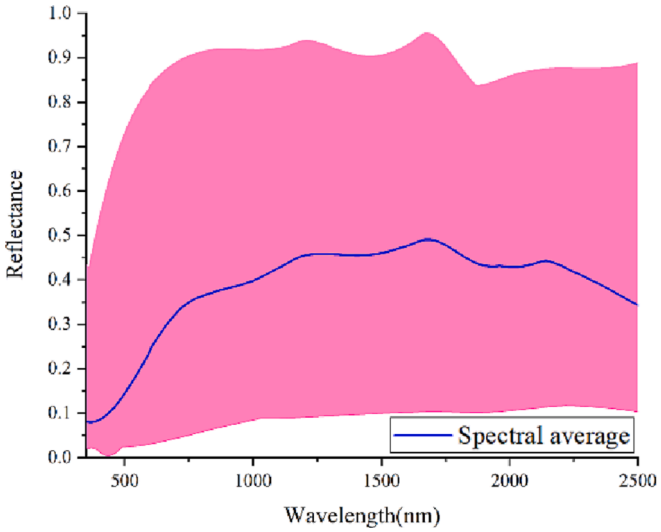

Fig. 6. Range of the selected spectra and the average spectrum.

4. Results

4.1. Soil property analysis

As shown in Fig. 7 a, the PSD shapes in the study area are mainly near-Gaussian and bimodal. Fig. 7 b shows that the soil taxonomy in the study area is mainly silt, silt loam, and silt clay loam, according to the United States Department of Agriculture (USDA) classification system, which divides the soil particle size into clay (≤2 μm), silt (2–50 μm), and sand (50–2000 μm).

Fig. 8 shows the PSD and spectra of the three layers of soil samples under one profile. The three layers of soil samples in this profile have similar SOM and iron oxide contents, and their spectra only correlate with the PSD. The mean particle size of the surface layer soil is significantly higher than that of the middle and bottom layers of the soil, so that the surface layer soil sample has the lowest spectral reflectance. The mean particle sizes of the middle and bottom layers are similar, but the fraction of the middle layer of soil is slightly higher in the larger particle size than the bottom layer, which results in the lower spectral reflectance for the middle layer. This phenomenon is compatible with the observation that the soil PSD affects the overall reflectance of the soil spectrum, and that the larger the soil particle size, the lower the spectral curve (Sadeghi et al. 2018).

Table 2 lists the chemical laboratory analysis results for the SOM and iron oxide contents. The soil iron oxide concentration increases with soil depth, and the SOM content decreases with the depth of soil, which is because soil iron oxide is mainly derived from the soil-forming parent material, and SOM is dependent on the formation of decaying surface humus.

As shown in Fig. 9, the three-dimensional spatial distribution map was produced using a kriging interpolation algorithm and overlaid with digital elevation model (DEM) data to better represent the distribution of the SOM and iron oxide contents of the soil profile for the whole study area. The DEM data were obtained from the ASTGTM2 DEM with a 30 m spatial resolution. The iron oxide content in the soil profile is correlated with topography, with the areas of high topography showing less variation than the areas of low topography. In contrast, the changes in SOM content are not significantly related to topography.

4.2. Spectral simulation performance of the SMRT model

The soil profile samples from each sampling site were used for independent modeling to ensure that the main influences on the laboratory spectra of the soil were only the SOM content, iron oxide content, and PSD. As the parameters fitted by the GA algorithm are not analytical solutions but acceptable local optima, the simulated spectra were noisy and needed to be denoised by Savitzky-Golay (SG) filtering. Fig. 10 shows an example of the simulated and denoised spectra of a soil sample.

Table 3 lists the spectral simulation accuracies of the different models. For the SMRT model, the simulation accuracy for the training set is$R^2 = 0.9841$, $RMSE = 0.0189$, and $MAE = 0.0101$, and the accuracy for the test set is $R^2 = 0.9343$, $RMSE = 0.0375$, and $MAE = 0.0279$. The simulation accuracies for the training and test sets are similar, which indicates that the SMRT model can adequately characterize the soil spectra. Fig. 11 shows a scatter plot of the reflectance simulation by the

Table 1
Statistics on the number of soil profiles and soil samples for each country.

Country	Profiles	Samples	Country	Profiles	Samples	Country	Profiles	Samples
Australia	19	158	India	3	16	Oman	1	5
Benin	3	21	Indonesia	25	167	Pakistan	4	26
Botswana	2	11	Ireland	4	24	Peru	12	75
Brazil	23	169	Italy	6	33	Philippines	2	10
Cameroon	1	7	Jamaica	2	14	Poland	9	56
China	28	222	Japan	2	25	Romania	3	27
Colombia	15	93	Kenya	15	98	Rwanda	1	6
Congo	1	5	Malaysia	11	87	Samoa	2	11
Cuba	16	94	Mali	5	43	Spain	13	92
Ecuador	8	46	Mozambique	6	37	Sweden	1	5
France	3	20	Namibia	3	18	Turkey	4	22
Gabon	4	22	Netherlands	12	101	Uruguay	7	37
Germany	5	43	Nicaragua	6	49	Zambia	6	76
Ghana	1	10	Niger	1	12	Zimbabwe	4	47
Greece	2	11	Nigeria	18	193			
Hungary	7	45	Norway	2	12			

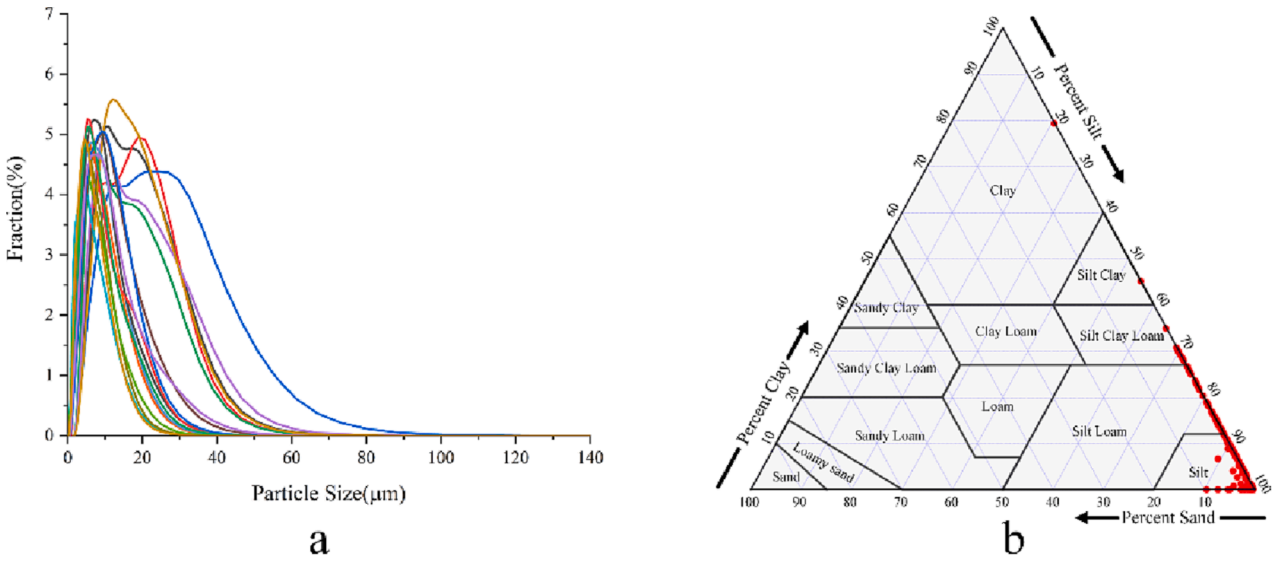

Fig. 7. A. the soil psds. b. the soil taxonomy.

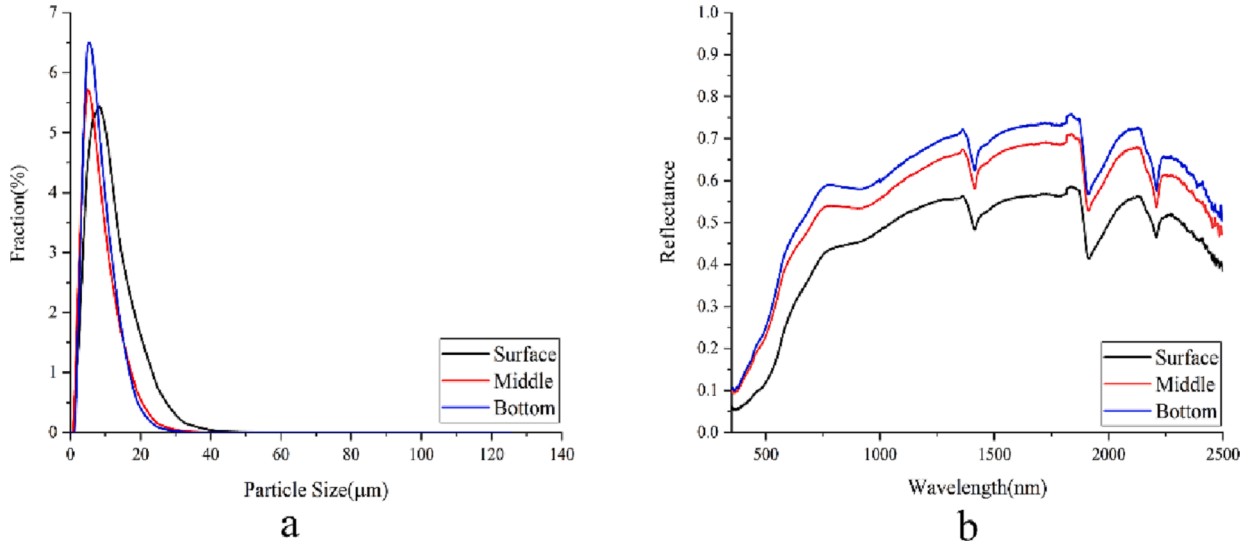

Fig. 8. PSDs and spectra of the three soil samples under one profile. a. PSDs. b. Spectra.

Table 2
The distributions of the SOM and soil iron oxide contents in the soil profile.

	SOM (g/kg)				Soil iron oxide (g/kg)			
	Mean	Max	Min	Sd	Mean	Max	Min	Sd
Surface	21.5721	37.9694	5.0861	6.9086	23.9814	36.7841	14.0854	4.3585
Middle	12.9541	26.3186	3.3106	5.9451	29.3236	48.7907	18.9651	6.2895
Bottom	11.5308	32.8971	1.5213	6.5495	30.7537	56.4263	14.6641	7.4191
Total	15.3523	37.9694	1.5213	7.8315	28.0196	56.4263	14.0854	6.7829

SMRT model. The points are in the region of the 1:1 line, which indicates that the SMRT model performs well in simulating the soil spectra. The spectral simulation accuracies of the KM and BT models considering a single factor are much lower than the accuracy of the SMRT model because the KM and BT models do not accurately describe the soil RT process under multi factors.

Fig. 12 shows the *RMSEP* of each band for all the samples. The *RMSEP* values decrease with the increasing wavelength up to 1000 nm in the visible range, while the *RMSEP* values are generally stable over 1000–2500 nm. The main reason for this is that the SMRT model is more capable of resolving the effects of soil particles in the SWIR wavelength than in the VNIR wavelength (Sadeghi et al. 2018). The superior spectral simulation accuracy provides the foundation for explaining the soil spectral features using the model parameters.

4.3. *Spectral simulation results based on the ICRAF-ISRIC spectral library*

The soil profile samples for each sampling site were used for independent modeling to ensure the consistency of the absorption and scattering coefficients. Table 4 lists the results corresponding to the

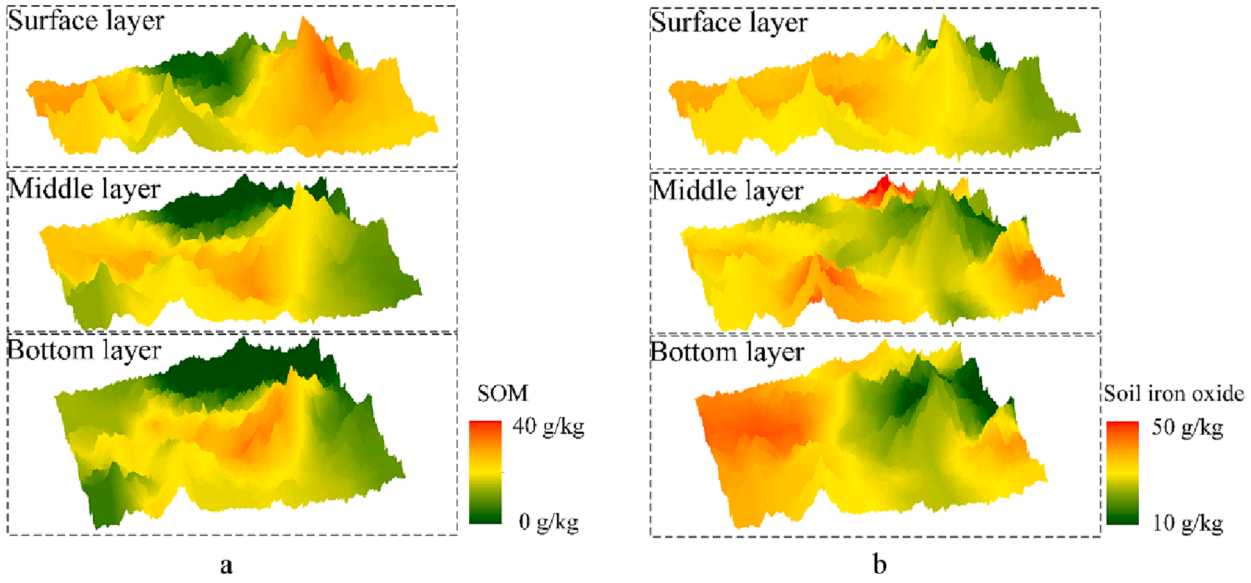

Fig. 9. Three-dimensional spatial distribution maps for SOM and soil iron oxide overlaid with DEM data. a. SOM. b. Soil iron oxide.

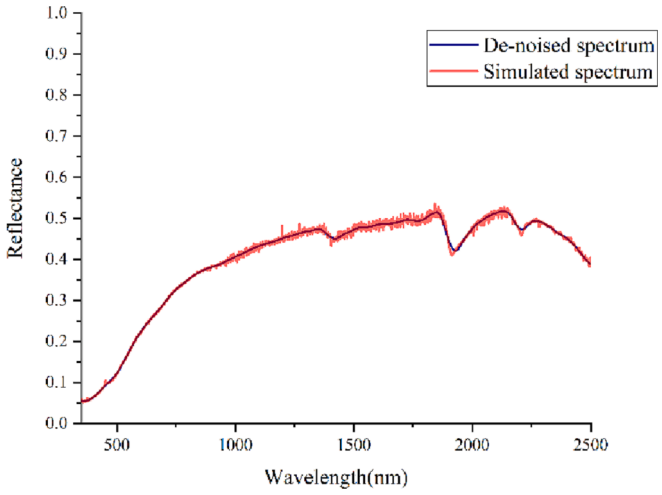

Fig. 10. Simulated spectrum (red line) and denoised spectrum (blue line) of a soil sample. (For interpretation of the references to color in this figure legend, the reader is referred to the web version of this article.)

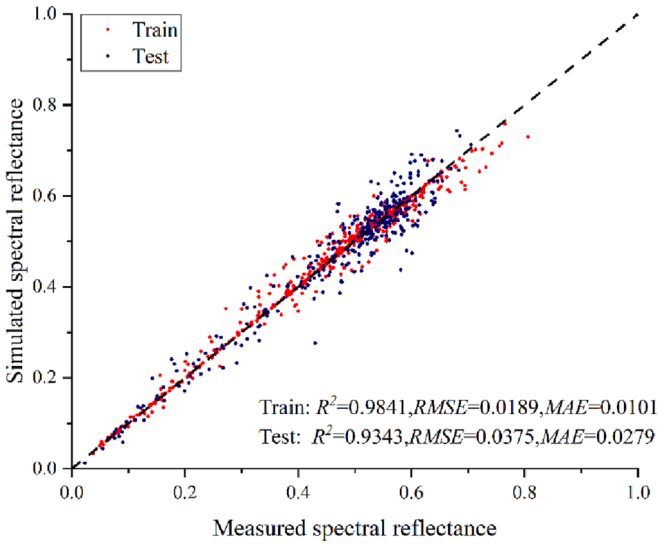

Fig. 11. Scatter plot of the reflectance simulation by the SMRT model.

Table 3
The spectral simulation accuracies of the different models.

Model	Training set			Test set		
	R^2	RMSE	MAE	R^2	RMSE	MAE
KM model	0.9793	0.0218	0.0154	0.6531	0.0802	0.0635
BT model	0.9767	0.0231	0.0158	0.6602	0.0794	0.0613
SMRT model	0.9841	0.0189	0.0101	**0.9343**	**0.0375**	**0.0279**

SMRT model based on the ICRAF-ISRIC spectral library. The overall accuracies of the simulated spectra are $R^2 = 0.8428$, $RMSE = 0.0605$, and $MAE = 0.0408$ for all the soil samples. The country with the highest spectral simulation accuracy is Sweden, with $R^2 = 0.9898$, $RMSE = 0.0085$, and $MAE = 0.0065$, and the country with the lowest accuracy is Jamaica. The particle size d_i in the SMRT model has been simplified to the estimated soil texture data, which caused a low accuracy in the spectral simulation. Fig. 13 illustrates the scatter plot corresponding to the measured reflectance and the simulated reflectance based on the SMRT model. The scatter plot shows a high correlation between the simulated reflectance and measured reflectance, with the points largely concentrating on the 1:1 line. In general, the SMRT model performs well with respect to the simulation of the ICRAF-ISRIC spectral library, which demonstrates the high generalization of the SMRT model.

5. Discussion

5.1. Features of the parameters based on the sampling data

The average of the SMRT model parameters for all the samples was calculated and smoothed to highlight the parameter features. The scattering and absorption coefficients of SOM in the SMRT model are shown in Fig. 14, where there is a very significant difference between K_{Som} and S_{Som} in the visible fraction. The combination of high scattering coefficients and low scattering absorption result in an increase in the absorption effect of light and a decrease in the scattering effect as the SOM content of the soil increases, which ultimately leads to a darker soil color (Ladoni et al. 2009). In addition, we define a band in which both K_{Som} and S_{Som} are at the peak or trough of the wave as an effective feature

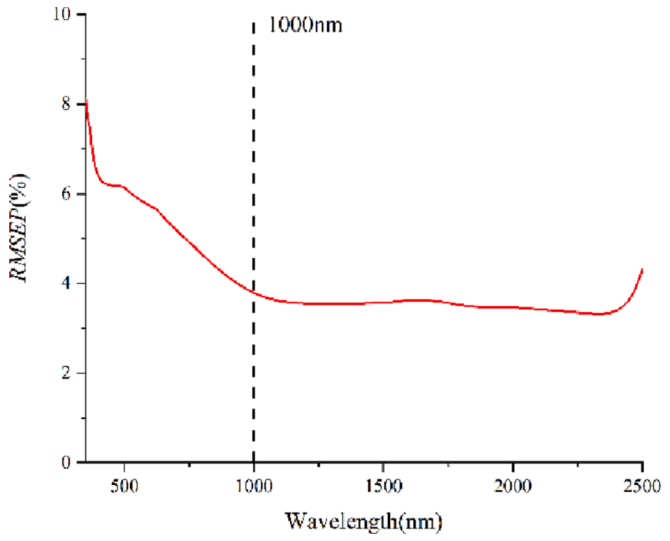

Fig. 12. The *RMSEP* of each band for all of the soil samples.

band. K_{Som} increases before 630 nm, while S_{Som} decreases, after which coefficient both tend to stabilize, which explains why the absorption feature band often used in SOM estimation studies is 630 nm (He et al. 2009, Stevens et al. 2013). Meanwhile, there are also significant peaks and troughs in K_{Som} and S_{Som} around 1840 nm, 1915 nm, 2130 nm, 2210 nm, and 2270 nm, implying that these bands are also effective feature bands, which are commonly used for SOM estimation (Madejova and Komadel 2001, Xu et al. 2020).

Table 5 presents a summary of the spectral feature wavelength assignments for the soil components, which can be used to explain the spectral features. SOM is a complicated combination with different compositions, so that the spectral feature wavelengths vary in different study areas. The main influential components of SOM for the spectral features are likely to be methyl, polysaccharides, and carbohydrates.

Table 6 lists the feature bands commonly used in SOM estimation. The feature bands used for estimating SOM are primarily concentrated around 350–780 nm, and the SMRT model shows that there are obvious features in the visible range with generally high absorption coefficients and low scattering coefficients.

Fig. 15 shows the relationship between the SOM absorption coefficient K_{Som} and scattering coefficient S_{Som}, which clearly reveals that K_{Som} and S_{Som} have a very high linear relationship (Pearson correlation coefficient $= -0.9363$) and a high fitting accuracy ($R^2 = 0.8767$).

As shown in Fig. 16, soil iron oxide shows a high absorption coefficient in the 350–550 nm range, and several studies have shown that the absorption features in this part of the spectrum are mainly caused by the ferrihydrite, goethite, hematite, and ferric oxide in the soil (Richter et al. 2009). There are also significant peaks and troughs around 1415 nm, 1915 nm, 2125 nm, 2210 nm, and 2270 nm, which are effective feature bands that are commonly used for soil iron oxide estimation. The absorption coefficient decreases and the scattering coefficient increases rapidly in the red wavelength range (550–750 nm). Thus, as the iron oxide in the soil increases, the scattering in the red wavelength range is enhanced and the soil color appears red, as in laterite soil.

The scattering coefficient for soil iron oxide increases with the wavelength up to 750 nm, and then stabilizes between 750 nm and 1915 nm, except around 1415 nm, where the scattering coefficient is lower (Krupnik and Khan 2019). As shown in Table 5, the main influential components of soil iron oxide for the spectral features are likely to be goethite, hematite, and hydroxyl.

Barrón and Torrent (1986) prepared hematite and synthetic goethite samples and measured the spectra at 400–700 nm. The absorption and scattering coefficients of iron oxide was then obtained by fitting the KM model. The absorption and scattering coefficients of soil iron oxide between 400 and 700 nm in the current study show similar trends to those of goethite. Ciani et al. (2005) obtained the absorption and scattering coefficients of goethite using the dilution method, which are similar to the results of the current study.

Table 4
Accuracies of the spectral simulation by the SMRT model based on the ICRAF-ISRIC spectral library.

Country	Training set			Test set		
	R^2	*RMSE*	*MAE*	R^2	*RMSE*	*MAE*
Australia	0.8891	0.0514	0.0357	0.8874	0.0499	0.0345
Benin	0.9585	0.0236	0.0165	0.9610	0.0236	0.0173
Botswana	0.8790	0.0409	0.0296	0.8639	0.0381	0.0248
Brazil	0.9287	0.0451	0.0299	0.9292	0.0452	0.0327
Cameroon	0.9803	0.0064	0.0043	0.9082	0.0137	0.0113
China	0.9052	0.0450	0.0304	0.8730	0.0515	0.0352
Colombia	0.9165	0.0433	0.0251	0.8986	0.0469	0.0334
Congo	0.9850	0.0106	0.0075	0.9197	0.0261	0.0165
Cuba	0.7338	0.0808	0.0539	0.5519	0.1062	0.0754
Ecuador	0.8598	0.0432	0.0332	0.8568	0.0412	0.0303
France	0.9292	0.0463	0.0361	0.8859	0.0554	0.0413
Gabon	0.9286	0.0352	0.0216	0.7409	0.0652	0.0454
Germany	0.7940	0.0652	0.0530	0.8097	0.0616	0.0480
Ghana	0.9566	0.0276	0.0233	0.9764	0.0197	0.0162
Greece	0.9406	0.0291	0.0236	0.9142	0.0355	0.0218
Hungary	0.8903	0.0443	0.0330	0.8491	0.0493	0.0405
India	0.9157	0.0438	0.0306	0.8529	0.0572	0.0463
Indonesia	0.8693	0.0561	0.0379	0.8230	0.0612	0.0383
Ireland	0.8407	0.0564	0.0433	0.8940	0.0454	0.0342
Italy	0.9727	0.0245	0.0181	0.9162	0.0429	0.0299
Jamaica	0.8128	0.0803	0.0544	0.5407	0.0968	0.0684
Japan	0.7293	0.0482	0.0360	0.7559	0.0436	0.0328
Kenya	0.9386	0.0318	0.0235	0.9112	0.0381	0.0258
Malaysia	0.7380	0.0794	0.0524	0.7184	0.0886	0.0546
Mali	0.8229	0.0613	0.0475	0.8383	0.0564	0.0419
Mozambique	0.7617	0.0646	0.0439	0.8494	0.0452	0.0297
Namibia	0.8816	0.0458	0.0280	0.9414	0.0297	0.0231
Netherlands	0.7458	0.0814	0.0608	0.7061	0.0840	0.0662
Nicaragua	0.7287	0.0785	0.0609	0.7660	0.0695	0.0547
Niger	0.9886	0.0160	0.0118	0.9861	0.0178	0.0118
Nigeria	0.8495	0.0566	0.0406	0.8474	0.0579	0.0415
Norway	0.8293	0.0501	0.0364	0.9164	0.0367	0.0259
Oman	0.5850	0.0849	0.0741	0.8233	0.0496	0.0422
Pakistan	0.9118	0.0302	0.0243	0.8732	0.0337	0.0255
Peru	0.8799	0.0570	0.0379	0.8004	0.0724	0.0494
Philippines	0.9853	0.0120	0.0103	0.9679	0.0174	0.0136
Poland	0.8705	0.0481	0.0356	0.7269	0.0708	0.0501
Romania	0.7673	0.0594	0.0512	0.6809	0.0729	0.0624
Rwanda	0.8933	0.0328	0.0260	0.9538	0.0191	0.0154
Samoa	0.9875	0.0131	0.0100	0.9743	0.0173	0.0132
Spain	0.7616	0.0710	0.0448	0.7422	0.0758	0.0513
Sweden	**0.9670**	**0.0150**	**0.0132**	**0.9898**	**0.0085**	**0.0065**
Turkey	0.8492	0.0580	0.0458	0.8055	0.0667	0.0494
Uruguay	0.8598	0.0515	0.0401	0.8790	0.0478	0.0346
Zambia	0.8892	0.0502	0.0363	0.8297	0.0640	0.0466
Zimbabwe	0.8818	0.0551	0.0381	0.8825	0.0567	0.0366
All_countries	**0.8707**	**0.0555**	**0.0375**	**0.8428**	**0.0605**	**0.0408**

Fig. 17 shows the relationship between the soil iron oxide absorption coefficient K_{SIO} and scattering coefficient S_{SIO}. Although the fitting parameters are not as accurate as those for SOM, they also show a high accuracy (Pearson correlation coefficient $= -0.9601$, $R^2 = 0.9214$).

Fig. 18 shows the values of the reflectance ρ and linear absorption coefficient k in the SMRT model as a function of wavelength. The reflectance ρ increases gradually with increasing wavelength, while the linear absorption coefficient k decreases with increasing wavelength up to 1500 nm, and then increases gradually after 1500 nm. The trends in the reflectance ρ and linear absorption coefficient k with wavelength are similar to those found by Sadeghi et al. (2015), and the linear absorption coefficients are significantly higher around 1415 nm, 1915 nm, and 2210 nm.

Fig. 19 illustrates the relationship between the reflectance and the linear absorption coefficient. The Pearson correlation coefficient between the reflectance and the linear absorption coefficient is −0.6657,

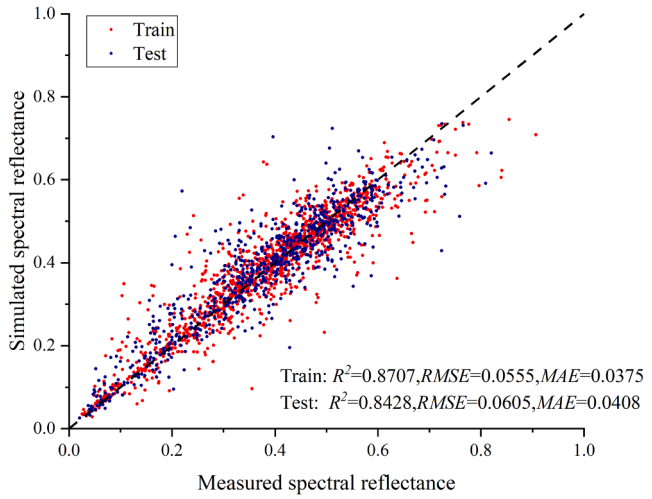

Fig. 13. Scatter plot of the reflectance simulation by the SMRT model based on the ICRAF-ISRIC spectral library.

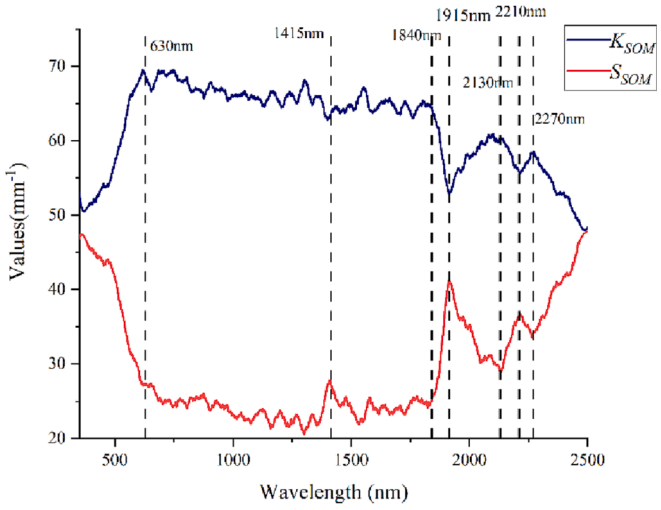

Fig. 14. The SOM absorption coefficient K_{Som} and scattering coefficient S_{Som} of each band.

Table 5
Feature wavelength assignments for soil components in the literature (Ben-Dor et al. 1997, Rossel and Behrens 2010).

Soil component		Wavelength (nm)
SOM	Aromatics	825, 1100, 1650
	Amine	751, 1000, 1500, 2060
	Carbohydrates	1449, 1930, 2381
	Amides	1524, 2033
	Methyl	1703–1852, 2307–2469
	Phenolics	1961
	Polysaccharides	2137
	Cellulose, lignin, starch, pectin	1260, 1367, 1468, 1660, 1730, 1769, 1780, 1932, 1950, 2142, 2331, 2337
	Urea, oil	2030, 2070, 2310, 2380
Soil iron oxide	Goethite	434, 480, 650, 920
	Hematite	404, 444, 529
	Hydroxyl	1400

which represents weak negative correlation. As the linear absorption coefficient k and the particle reflectance ρ are the inherent properties of a soil particle, there is no correlation between these two parameters.

In contrast, the absorption and scattering coefficients of soil particles

Table 6
Summary of the feature wavelengths for estimating SOM.

Reference	Wavelength (nm)	Method
He et al. (2009)	587, 845, 863, 905, 1500, 1681, 1740, 2137, 2187	Linear regression
Liu et al. (2014)	350–800, 1900	Partial least squares regression
Hong et al. (2019)	410, 500, 510, 530, 570, 580, 590, 670, 690, 710, 750, 810, 820, 830, 930, 940,950, 1400, 1920, 2390	Memory-based learning
Xu et al. (2020)	800, 1000, 1100, 1200, 1420, 1500, 1800, 1920, 2000, 2100, 2200, 2350	Partial least squares regression
Meng et al. (2021)	488, 531, 598, 1485, 1511, 1536	Random forest
Ou et al. (2021)	570, 670, 750, 890, 1100, 2210	Semi-supervised deep neural network regression

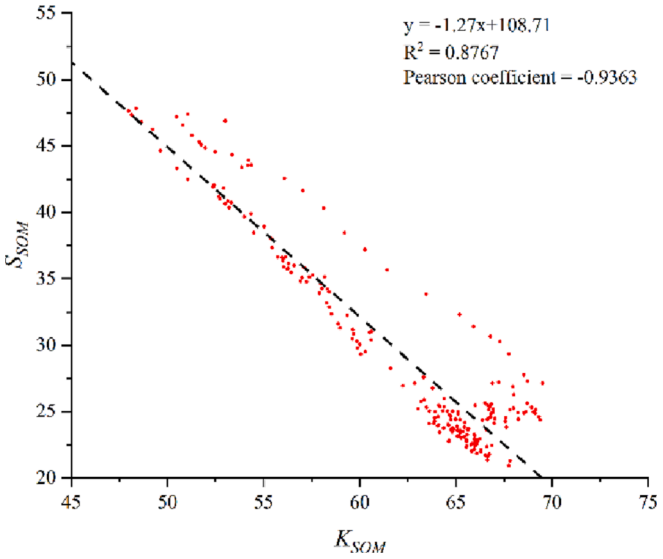

Fig. 15. Correlation between the SOM absorption coefficient K_{Som} and scattering coefficient S_{Som}.

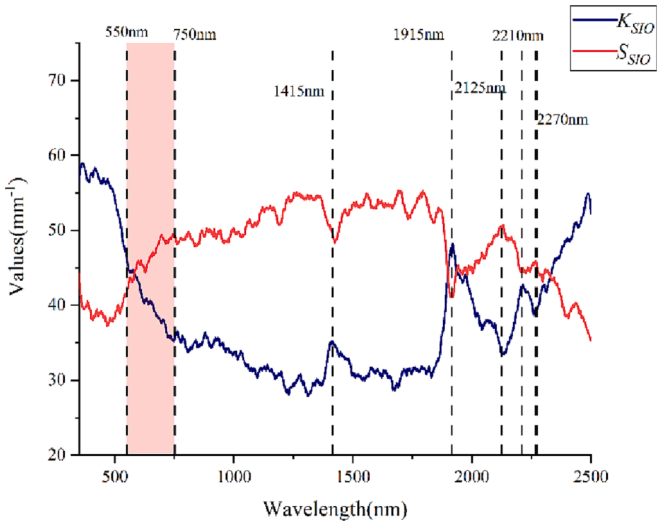

Fig. 16. The soil iron oxide absorption coefficient K_{SIO} and scattering coefficient S_{SIO} of each band.

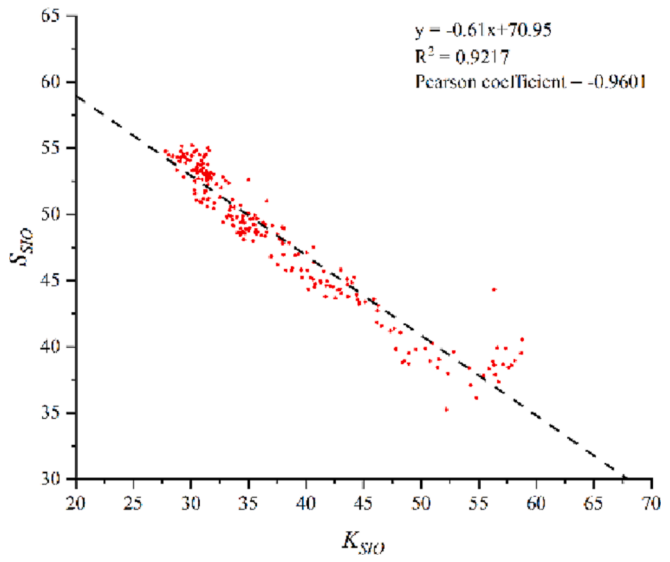

Fig. 17. Correlation of the soil iron oxide absorption coefficient K_{SIO} and scattering coefficient S_{SIO}.

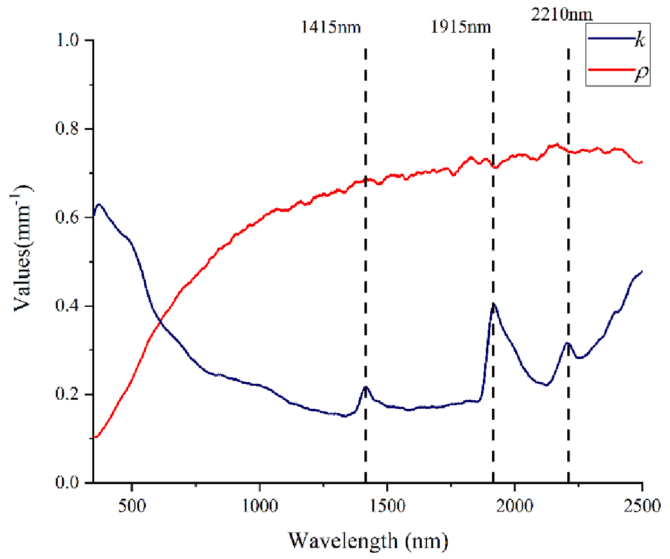

Fig. 18. The particle reflectance ρ and linear absorption coefficient k of each band.

calculated from the linear absorption coefficient k and the particle reflectance ρ have a strong correlation. Fig. 20 shows the values of the soil particle absorption coefficient K_{Par} and scattering coefficient S_{Par} in the SMRT model as a function of wavelength. The absorption coefficient K_{Par} and linear absorption coefficient k show similar trends for 350–2500 nm, as do the scattering coefficient S_{Par} and reflectance ρ, which is mainly because the absorption and scattering coefficients of the soil particles are calculated cumulatively for multiple single particles.

However, unlike a single particle, the absorption and scattering coefficients of soil particles have a strong correlation. As shown in Fig. 21, K_{Par} and S_{Par} have a very high linear relationship (Pearson correlation coefficient = −0.9778) and a high fitting accuracy (R^2 = 0.9561).

In infinitely thick soils, the RT process can be summarized as an absorption effect and a scattering effect, which are antagonistic. Thus, the absorption and scattering coefficients of SOM, soil particles, and iron oxide calculated by the SMRT model all have a very strong negative correlation, which laterally verifies the accuracy of the SMRT model in describing the spectral response mechanism of soils.

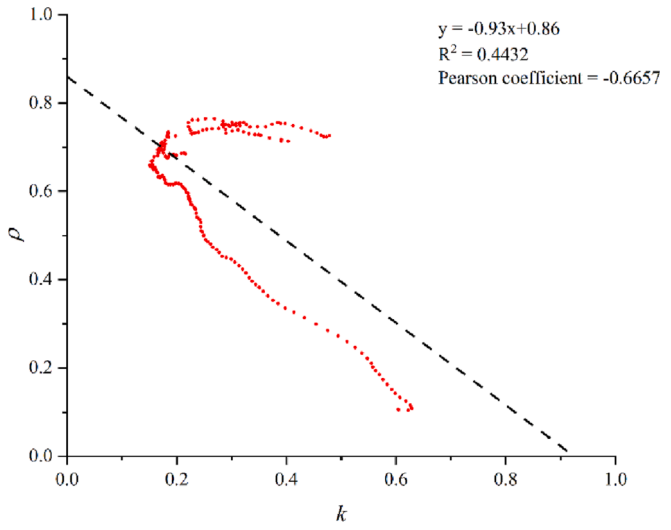

Fig. 19. Correlation between the particle reflectance ρ and linear absorption coefficient k.

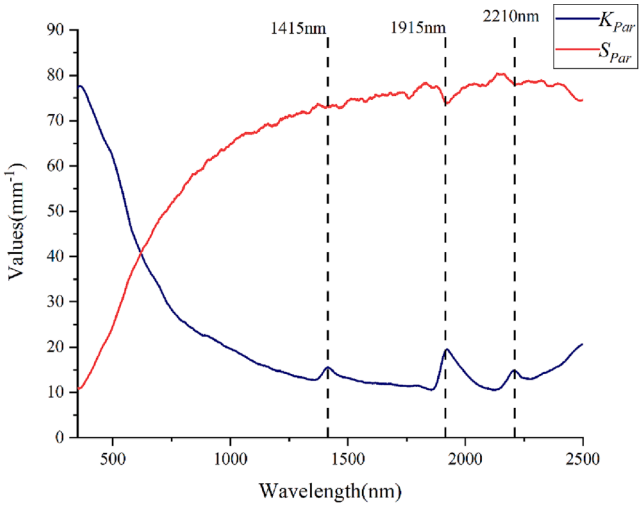

Fig. 20. Soil particle absorption coefficient K_{Par} and scattering coefficient S_{Par} of each band.

5.2. Features of the parameters based on the ICRAF-ISRIC spectral library

Fig. 22 shows the relationship between the absorption and scattering coefficients of SOM, soil iron oxide, and soil particles, respectively. The absorption and scattering coefficients of soil particles have a strong negative correlation. In contrast, the absorption and scattering coefficients of SOM and soil iron oxide show a weak negative correlation. The correlation between the absorption and scattering coefficients is inferior to the results described in Section 5.1. As the ICRAF-ISRIC spectral library covers a wider range of soil types around the world (Cao et al. 2020), the correlation between the absorption and scattering coefficients is of more universality.

5.3. Spatial variation of the absorption and scattering coefficients based on the ICRAF-ISRIC spectral library

As the absorption and scattering coefficients are wavelength dependent, it is impossible to list all the absorption and scattering coefficients of soil samples in the ICRAF-ISRIC spectral library. The absorption and scattering coefficients of the feature bands for SOM (630 nm) and soil iron oxide (750 nm) were chosen to investigate their spatial

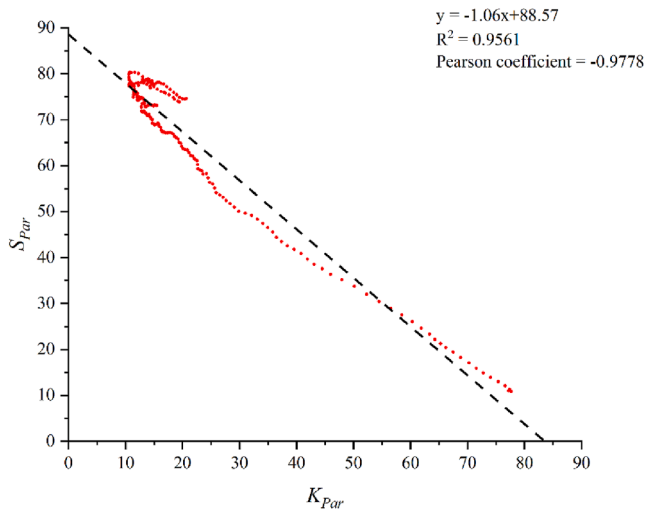

Fig. 21. Correlation between the soil particle absorption coefficient K_{Par} and scattering coefficient S_{Par}.

variation. Table 7 lists the statistics for the absorption and scattering coefficients of SOM and soil iron oxide. The coefficient of variation (C.V.) shows that the variation in SOM is significantly greater than that in soil iron oxide. The absorption and scattering coefficients are dependent on the composition, and the composition of SOM is more complex than that of soil iron oxide, which causes differences in the spatial variation of the coefficients of SOM and soil iron oxide.

The global Moran index (Moran's I) is introduced to measure the spatial heterogeneity of the coefficients. As listed in Table 8, all the coefficients have small Moran's I values, with p-values greater than 0.1, indicating that the coefficients are randomly distributed and there is no significant spatial autocorrelation.

5.4. The reduced-parameter SMRT model

According to the above results, the high correlation of the absorption

Table 7
The statistics for the absorption and scattering coefficients.

	Max	Min	Mean	Sd	C.V.
K_Som	87.4574	32.8273	56.5206	9.7591	0.1726
S_Som	72.3924	8.7099	40.3152	10.0794	0.2501
K_SIO	75.8630	25.3473	50.8401	7.9503	0.1563
S_SIO	67.2922	28.4951	48.4885	7.0754	0.1459

Table 8
The global Moran's I statistics for the absorption and scattering coefficients.

	Moran's I	Z-score	P-value
K_Som	−0.0172	−0.9848	0.3247
S_Som	0.0099	0.9071	0.3644
K_SIO	0.0051	0.5659	0.5714
S_SIO	0.0076	0.7472	0.4548

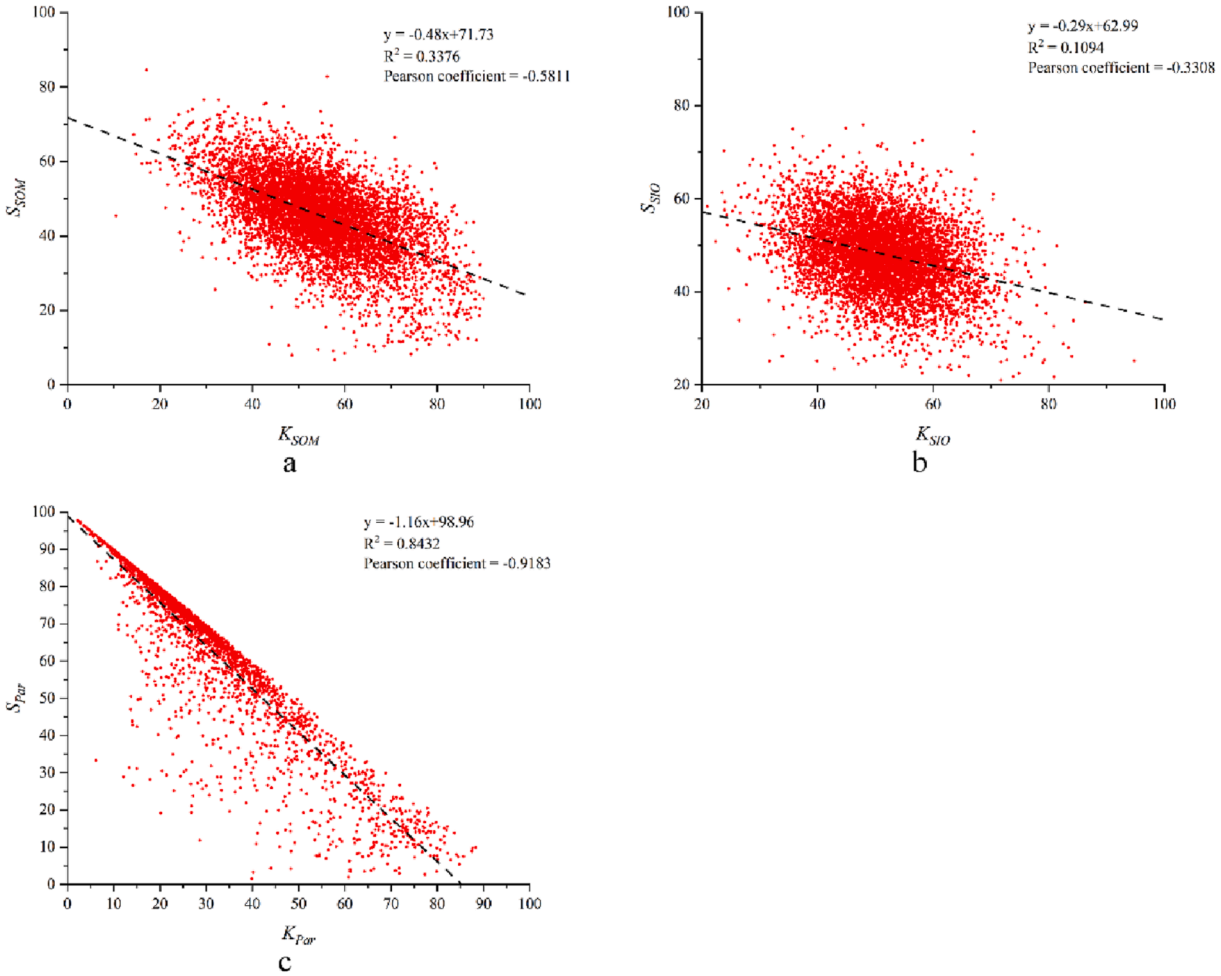

Fig. 22. Correlation between the absorption and scattering coefficients based on the ICRAF-ISRIC spectral library. a. SOM. b. Soil iron oxide. c. Soil particles.

and scattering coefficients for SOM and soil iron oxide makes it possible to further simplify the model by reducing the number of model parameters. Based on the results of the sampling point data, the scattering coefficients for SOM and soil iron oxide can be expressed as:

$$S_{Som} = -1.27K_{Som} + 108.71 \quad (21)$$

$$S_{SIO} = -0.61K_{SIO} + 70.95 \quad (22)$$

The parameters remaining to be solved in the SMRT model are then the soil particle optical coefficients (ρ and k), and absorption coefficients (K_{SOM} and K_{SIO}), which greatly decreases the complexity, compared with the previous six parameters.

Table 9 lists the results for the simplified SMRT model, where the spectral simulation accuracy is similar to that of the original SMRT model.

However, the absorption and scattering coefficients depend on the composition of the soil constituents, and the above relationships for absorption and scattering coefficients only represent the characteristics in the study area.

As the ICRAF-ISRIC spectral library covers a global range of soil types, the correlations between the absorption and scattering coefficients in the ISRIC spectral library will have greater universality. Thus, based on the results of the ICRAF-ISRIC spectral library, the scattering coefficients for SOM and soil iron oxide can be expressed as:

$$S_{Som} = -0.48K_{Som} + 71.73 \quad (23)$$

$$S_{SIO} = -0.29K_{SIO} + 62.99 \quad (24)$$

As shown in Table 10, the spectral simulation accuracies are over 0.8 in R^2 for both datasets. The parameters in Equations (23) and (24) are more representative and general, which means that they can be used as empirical values to reduce the number of SMRT model parameters.

Table 9
The statistical results for the simplified SMRT model based on the results of the sampling point data.

	R^2	*RMSE*	*MAE*
Training set	0.9851	0.0189	0.0094
Test set	0.9301	0.0394	0.0296
All data	0.9667	0.0271	0.0161

Table 10
The statistical results for the simplified SMRT model based on the results of the ICRAF-ISRIC spectral library.

Dataset		R^2	*RMSE*	*MAE*
Sampling points	Training set	0.9822	0.0193	0.0102
	Test set	0.9139	0.0421	0.0315
	All data	0.9599	0.0289	0.0173
ICRAF-ISRIC	Training set	0.8222	0.0603	0.0418
	Test set	0.8213	0.0604	0.0411
	All data	0.8219	0.0603	0.0415

6. Conclusion

The SMRT model takes full account of the main influencing factors for soil spectra, i.e., the PSD, SOM content, and iron oxide content. Although the model makes some simplifying assumptions, such as ignoring the diffraction and dispersion of light, assuming light isotropy, etc., to improve the robustness, the experimental results showed that the model achieved a high simulation accuracy for the different types of soil spectra in the study area. In addition, the soil profile dataset used in the experiments can illustrate the practical application of the SMRT model, compared to controlled variable experiments in the laboratory, while ensuring that the soil-forming parent material is consistent under a soil profile and that the main influences on the soil spectra are only PSD, SOM content, and iron oxide content.

The derived parameters of the SMRT model provide a theoretical basis for indicator content estimation using soil spectra. The absorption and scattering coefficients in the model further corroborate the physical mechanism of the sensitive spectral features of the soil indicators in previous studies. The spectral feature wavelength bands identified in this study agree with the general wavelength ranges but were not the same as the previous study findings, and the reason for this is that the effect of soil components on the spectra is not a single wavelength band but a specific range of effects. Thus, the similar feature range indicates that the SMRT model can correctly explain the spectral features through the spectral mechanism. The SMRT model parameters also explain the color representation of black soil and laterite soil from the RT process.

Further analysis of the model parameters indicated that the spectral features around 1910 nm and 2210 nm are specific. These two spectral features are often interpreted as being caused by the SM and clay mineral content (St. Luce et al. 2014). Analysis of the absorption and scattering coefficients demonstrated that the spectral features around 1910 nm and 2210 nm are not only caused by these two factors, but several factors, including the SOM, iron oxide content, and PSD. However, the concentration of SM and clay minerals is much higher than that of SOM and iron oxide, resulting in the spectral features of clay minerals and moisture masking the other factors, which has led to the data-driven models used in the previous studies only illustrating the effects of moisture and clay minerals.

This study focused on the theoretical aspects of the model and verified its feasibility under optimal indoor experimental conditions. However, as the coefficients in the SMRT model are dependent on the soil properties, the coefficients cannot be constants. The requirement to calibrate the model parameters by samples in practical applications limits the application of the SMRT model. Future studies should combine DEM data and soil texture data to address more severe conditions in hyperspectral imagery, such as topographic shadow effects, mixed image elements, and so on, which will help the model overcome the current application limitations and expand its application to hyperspectral imagery.

CRediT authorship contribution statement

Fuyu Wu: Methodology, Data curation, Writing – original draft. **Kun Tan:** Conceptualization, Resources, Writing – review & editing. **Xue Wang:** Methodology, Writing – review & editing. **Jianwei Ding:** Supervision. **Zhaoxian Liu:** Investigation. **Bo Han:** Resources.

Declaration of Competing Interest

The authors declare that they have no known competing financial interests or personal relationships that could have appeared to influence the work reported in this paper.

Data availability

Data will be made available on request.

Acknowledgements

This research is jointly supported by the National Natural Science Foundation of China (Grant No. 42171335), the Shanghai Municipal Science and Technology Major Project (No. 22511102800) and the National Civil Aerospace Project of China (Grant No. D040102).

References

Angelopoulou, T., Tziolas, N., Balafoutis, A., Zalidis, G., Bochtis, D., 2019. Remote Sensing Techniques for Soil Organic Carbon Estimation: A Review. Remote Sens. (Basel) 11 (6), 676.

Anne, N.J.P., Abd-Elrahman, A.H., Lewis, D.B., Hewitt, N.A., 2014. Modeling soil parameters using hyperspectral image reflectance in subtropical coastal wetlands. Int. J. Appl. Earth Observ. Geoinform. 33, 47–56.
Bablet, A., Vu, P.V.H., Jacquemoud, S., Viallefont-Robinet, F., Fabre, S., Briottet, X., Sadeghi, M., Whiting, M.L., Baret, F., Tian, J., 2018. MARMIT: A multilayer radiative transfer model of soil reflectance to estimate surface soil moisture content in the solar domain (400–2500 nm). Remote Sens. Environ. 217, 1–17.
Banninger, D., Fluhler, H., 2004. Modeling light scattering at soil surfaces. IEEE Trans. Geosci. Remote Sens. 42 (7), 1462–1471.
Barrón, V., Torrent, J., 1986. Use of the Kubelka—Munk theory to study the influence of iron oxides on soil colour. J. Soil Sci. 37 (4), 499–510.
Ben-Dor, E., Inbar, Y., Chen, Y., 1997. The reflectance spectra of organic matter in the visible near-infrared and short wave infrared region (400–2500 nm) during a controlled decomposition process. Remote Sens. Environ. 61 (1), 1–15.
Benedet, L., Faria, W.M., Silva, S.H.G., Mancini, M., Demattê, J.A.M., Guilherme, L.R.G., Curi, N., 2020. Soil texture prediction using portable X-ray fluorescence spectrometry and visible near-infrared diffuse reflectance spectroscopy. Geoderma. 376, 114553.
Cai, H.-T., Liu, J., Chen, J.-Y., Zhou, K.-H., Pi, J., Xia, L.-R., 2021. Soil nutrient information extraction model based on transfer learning and near infrared spectroscopy. Alex. Eng. J. 60 (3), 2741–2746.
Cao, R., Feng, Y., Liu, X., Shen, M., Zhou, J., 2020. Uncertainty of vegetation green-up date estimated from vegetation indices due to snowmelt at northern middle and high latitudes. Remote Sens. (Basel) 12 (1), 190.
Chen, L., Lai, J., Tan, K., Wang, X., Chen, Y., Ding, J., 2022. Development of a soil heavy metal estimation method based on a spectral index: Combining fractional-order derivative pretreatment and the absorption mechanism. Sci Total Environ. 813, 151882.
Chen, H., Ma, Y., Zhu, A., Wang, Z., Zhao, G., Wei, Y., 2021. Soil salinity inversion based on differentiated fusion of satellite image and ground spectra. Int. J. Appl. Earth Observ. Geoinform. 101, 102360.
Christy, A.A., Kvalheim, O.M., Velapoldi, R.A., 1995. Quantitative analysis in diffuse reflectance spectrometry: a modified Kubelka-Munk equation. Vib. Spectrosc 9 (1), 19–27.
Ciani, A., Goss, K.U., Schwarzenbach, R.P., 2005. Light penetration in soil and particulate minerals. Eur. J. Soil Sci. 56 (5), 561–574.
Demattê, J.A.M., da Silva Terra, F., 2014. Spectral pedology: A new perspective on evaluation of soils along pedogenetic alterations. Geoderma. 217, 190–200.
Ding, A., Ma, H., Liang, S., He, T., 2022. Extension of the Hapke model to the spectral domain to characterize soil physical properties. Remote Sens. Environ. 269, 112843.
Garrity, D., Bindraban, P., 2004. A globally distributed soil spectral library visible near infrared diffuse reflectance spectra. ICRAF (World Agroforestry Centre)/ISRIC (World Soil Information) Spectral Library: Nairobi, Kenya.
He, T., Wang, J., Lin, Z., Cheng, Y., 2009. Spectral features of soil organic matter. Geospatial Inform. Sci. 12 (1), 33–40.
Holland, J.H., 1992. Genetic algorithms. Sci. American 267 (1), 66–73.
Hong, Y., Chen, S., Liu, Y., Zhang, Y., Yu, L., Chen, Y., Liu, Y., Cheng, H., Liu, Y., 2019. Combination of fractional order derivative and memory-based learning algorithm to improve the estimation accuracy of soil organic matter by visible and near-infrared spectroscopy. Catena 174, 104–116.
Jacquemoud, S., Baret, F., Hanocq, J.F., 1992. Modeling spectral and bidirectional soil reflectance. Remote Sens. Environ. 41 (2–3), 123–132.
Janik, L.J., Soriano-Disla, J.M., Forrester, S.T., 2020. Feasibility of handheld mid-infrared spectroscopy to predict particle size distribution: influence of soil field condition and utilisation of existing spectral libraries. Soil Res. 58 (6), 528.
Jeong, Y., Yu, J., Wang, L., Lee, K.-J., 2021. Bulk scanning method of a heavy metal concentration in tailings of a gold mine using SWIR hyperspectral imaging system. Int. J. Appl. Earth Observ. Geoinform. 102, 102382.
Katoch, S., Chauhan, S.S., Kumar, V., 2021. A review on genetic algorithm: past, present, and future. Multimed. Tools Appl. 80 (5), 8091–8126.
Koch, M., Schodlok, M.C., Guggenberger, G., Stadler, S., 2021. Effects of water tension and surface roughness on soil hyperspectral reflectance. Geoderma. 385, 114888.
Krupnik, D., Khan, S., 2019. Close-range, ground-based hyperspectral imaging for mining applications at various scales: Review and case studies. Earth Sci. Rev. 198, 102952.
Labarre, S., Ferrari, C., Jacquemoud, S., 2017. Surface roughness retrieval by inversion of the Hapke model: A multiscale approach. Icarus 290, 63–80.
Ladoni, M., Bahrami, H.A., Alavipanah, S.K., Norouzi, A.A., 2009. Estimating soil organic carbon from soil reflectance: a review. Precis. Agric. 11 (1), 82–99.
Liang, S., Townshend, J.R., 1996. A modified Hapke model for soil bidirectional reflectance. Remote Sens. Environ. 55 (1), 1–10.
Liu, M., Han, G., Zhang, Q., 2020. Effects of agricultural abandonment on soil aggregation, soil organic carbon storage and stabilization: Results from observation in a small karst catchment, Southwest China. Agr Ecosyst Environ 288, 106719.
Liu, Y., Jiang, Q., Fei, T., Wang, J., Shi, T., Guo, K., Li, X., Chen, Y., 2014. Transferability of a visible and near-infrared model for soil organic matter estimation in riparian landscapes. Remote Sens. (Basel) 6 (5), 4305–4322.
Liu, Y., Shi, Z., Zhang, G., Chen, Y., Li, S., Hong, Y., Shi, T., Wang, J., Liu, Y., 2018. Application of Spectrally Derived Soil Type as Ancillary Data to Improve the Estimation of Soil Organic Carbon by Using the Chinese Soil Vis-NIR Spectral Library. Remote Sens. (Basel) 10 (11), 1747.
Madejova, J., Komadel, P., 2001. Baseline studies of the clay minerals society source clays: infrared methods. Clay Clay Miner. 49 (5), 410–432.
Meng, X., Bao, Y., Ye, Q., Liu, H., Zhang, X., Tang, H., Zhang, X., 2021. Soil organic matter prediction model with satellite hyperspectral image based on optimized denoising method. Remote Sens. (Basel) 13 (12), 2273.
Norouzi, S., Sadeghi, M., Liaghat, A., Tuller, M., Jones, S.B., Ebrahimian, H., 2021. Information depth of NIR/SWIR soil reflectance spectroscopy. Remote Sens. Environ. 256, 112315.
Ou, D., Tan, K., Lai, J., Jia, X., Wang, X., Chen, Y., Li, J., 2021. Semi-supervised DNN regression on airborne hyperspectral imagery for improved spatial soil properties prediction. Geoderma. 385, 114875.
Peng, J., Biswas, A., Jiang, Q., Zhao, R., Hu, J., Hu, B., Shi, Z., 2019. Estimating soil salinity from remote sensing and terrain data in southern Xinjiang Province, China. Geoderma. 337, 1309–1319.
Richter, N., Jarmer, T., Chabrillat, S., Oyonarte, C., Hostert, P., Kaufmann, H., 2009. Free Iron Oxide Determination in Mediterranean Soils using Diffuse Reflectance Spectroscopy. Soil Sci. Soc. Am. J. 73 (1), 72–81.
Rossel, R.A.V., Behrens, T., 2010. Using data mining to model and interpret soil diffuse reflectance spectra. Geoderma. 158 (1–2), 46–54.
Rossel, R., Behrens, T., Ben-Dor, E., Brown, D., Dematte, J., Shepherd, K., Shi, Z., Stenberg, B., Stevens, A., Adamchuk, V., Aichi, H., Barthes, B., Bartholomeus, H., Bayer, A., Bernoux, M., Bottcher, K., Brodsky, L., Du, C., Chappell, A., Fouad, Y., Genot, V., Gomez, C., Grunwald, S., Gubler, A., Guerrero, C., Hedley, C., Knadel, M., Morras, H., Nocita, M., Ramirez-Lopez, L., Roudier, P., Campos, E., Sanborn, P., Sellitto, V., Sudduth, K., Rawlins, B., Walter, C., Winowiecki, L., Hong, S., Ji, W., 2016. A global spectral library to characterize the world's soil. Earth Sci. Rev. 155, 198–230.
Sadeghi, M., Jones, S.B., Philpot, W.D., 2015. A linear physically-based model for remote sensing of soil moisture using short wave infrared bands. Remote Sens. Environ. 164, 66–76.
Sadeghi, M., Babaeian, E., Tuller, M., Jones, S.B., 2018. Particle size effects on soil reflectance explained by an analytical radiative transfer model. Remote Sens. Environ. 210, 375–386.
Sawut, R., Kasim, N., Abliz, A., Hu, L., Yalkun, A., Maihemuti, B., Qingdong, S., 2018. Possibility of optimized indices for the assessment of heavy metal contents in soil around an open pit coal mine area. Int. J. Appl. Earth Observ. Geoinform. 73, 14–25.
Shirazi, M.A., Boersma, L., 1984. A unifying quantitative analysis of soil texture. Soil Sci. Soc. Am. J. 48 (1), 142–147.
Song, L., Jian, J., Tan, D.-J., Xie, H.-B., Luo, Z.-F., Gao, B., 2015. Estimate of heavy metals in soil and streams using combined geochemistry and field spectroscopy in Wan-sheng mining area, Chongqing, China. Int. J. Appl. Earth Observ. Geoinform. 34, 1–9.
St. Luce, M., Ziadi, N., Zebarth, B.J., Grant, C.A., Tremblay, G.F., Gregorich, E.G., 2014. Rapid determination of soil organic matter quality indicators using visible near infrared reflectance spectroscopy. Geoderma 232–234, 449–458.
Stenberg, B., Viscarra Rossel, R.A., Mouazen, A.M., Wetterlind, J., 2010. Visible and Near Infrared Spectroscopy in Soil Science. Adv. Agron. 107, 163–215.
Stevens, A., Nocita, M., Toth, G., Montanarella, L., van Wesemael, B., 2013. Prediction of Soil Organic Carbon at the European Scale by Visible and Near InfraRed Reflectance Spectroscopy. PLoS One. 8 (6), e66409.
Sun, W., Zhang, X., 2017. Estimating soil zinc concentrations using reflectance spectroscopy. Int. J. Appl. Earth Observ. Geoinform. 58, 126–133.
Tan, K., Ma, W., Chen, L., Wang, H., Du, Q., Du, P., Yan, B., Liu, R., Li, H., 2021. Estimating the distribution trend of soil heavy metals in mining area from HyMap airborne hyperspectral imagery based on ensemble learning. J Hazard Mater. 401, 123288.
Vargas, W.E., Niklasson, G.A., 1997. Applicability conditions of the Kubelka-Munk theory. Appl. Opt. 36 (22), 5580–5586.
Wang, F., Gao, J., Zha, Y., 2018. Hyperspectral sensing of heavy metals in soil and vegetation: Feasibility and challenges. ISPRS J. Photogramm. Remote Sens. 136, 73–84.
Wang, J., He, T., Lv, C., Chen, Y., Jian, W., 2010. Mapping soil organic matter based on land degradation spectral response units using Hyperion images. Int. J. Appl. Earth Observ. Geoinform. 12, S171–S180.
Wei, L., Ge, T., Zhu, Z., Luo, Y., Yang, Y., Xiao, M., Yan, Z., Li, Y., Wu, J., Kuzyakov, Y., 2021. Comparing carbon and nitrogen stocks in paddy and upland soils: Accumulation, stabilization mechanisms, and environmental drivers. Geoderma. 398, 115121.
Xu, L., Hong, Y., Wei, Y., Guo, L., Shi, T., Liu, Y., Jiang, Q., Fei, T., Liu, Y., Mouazen, A. M., Chen, Y., 2020. Estimation of Organic Carbon in Anthropogenic Soil by VIS-NIR Spectroscopy: Effect of Variable Selection. Remote Sens. (Basel) 12 (20), 3394.
Yin, F., Wu, M., Liu, L., Zhu, Y., Feng, J., Yin, D., Yin, C., Yin, C., 2021. Predicting the abundance of copper in soil using reflectance spectroscopy and GF5 hyperspectral imagery. Int. J. Appl. Earth Observ. Geoinform. 102, 102420.
Zhang, Y., Tan, K., Wang, X., Chen, Y., 2020. Retrieval of Soil Moisture Content Based on a Modified Hapke Photometric Model: A Novel Method Applied to Laboratory Hyperspectral and Sentinel-2 MSI Data. Remote Sens. (Basel) 12 (14), 2239.